Cell shape and substrate stiffness drive actin-based cell polarity

Mukund Gupta,[1,2,*] Bryant L. Doss,[1] Leyla Kocgozlu,[1] Meng Pan,[1] René-Marc Mège,[2] Andrew Callan-Jones,[3] Raphaël Voituriez,[4,5,†] and Benoît Ladoux[1,2,‡]

[1]*Mechanobiology Institute, National University of Singapore, 117411 Singapore, Singapore*
[2]*Institut Jacques Monod, CNRS, UMR No. 7592, Université Paris Diderot, 75013 Paris, France*
[3]*Laboratoire Matière et Systèmes Complexes, UMR No. 7057 CNRS, Université Paris Diderot, 75013 Paris, France*
[4]*Laboratoire de Physique Théorique de la Matière Condensée, CNRS, UPMC, 4 Place Jussieu, 75005 Paris, France*
[5]*Laboratoire Jean Perrin, CNRS, UPMC, 4 Place Jussieu, 75005 Paris, France*

(Received 3 March 2018; published 10 January 2019)

A general trait of living cells is their ability to exert contractile stresses on their surroundings and thus respond to substrate rigidity. At the cellular scale, this response affects cell shape, polarity, and ultimately migration. The regulation of cell shape together with rigidity sensing remains largely unknown. In this article we show that both substrate rigidity and cell shape contribute to drive actin organization and cell polarity. Increasing substrate rigidity affects bulk properties of the actin cytoskeleton by favoring long-lived actin stress fibers with increased nematic interactions, whereas cell shape imposes a local alignment of actin fibers at the cell periphery.

DOI: 10.1103/PhysRevE.99.012412

I. INTRODUCTION

Cell polarity, or the asymmetric organization of cellular components, is essential for tissue development and function [1–3]. Notably, polarized cell migration is fundamental in tissue morphogenesis, wound healing, and pathological states such as cancer [4,5]. One of the main drivers of front-rear polarity of a migrating cell is the symmetry breaking and polarization of the actin cytoskeleton [6–9]. This process depends on the mechanical properties of the surrounding extracellular matrix (ECM) and the orientation of adhesion complexes and traction forces [7,10–12]. On stiff substrates, cells adopt polarized shapes and nematic ordering of the actin cytoskeleton with stable stress fibers coupled directly to focal adhesions (FAs) [11,13,14]. However, on softer substrates, cells are circular in shape and the actin cytoskeleton is highly dynamic as fibers aligned along the cell boundary flow towards the cell center [11,13]. Previously, we had proposed a coarse-grained description of this change in actin cytoskeleton organization under the framework of active gel theory as a transition from an isotropic to a nematic phase induced by substrate stiffness [13]. However, the coupling to cell shape remains largely unexplored, even though FA dynamics and traction forces, which are critically controlled by ECM stiffness [10,15,16], have been suggested to play an important role in defining cell shape [17,18]. Thus there appears to be interplay between cell shape and actin organization that varies as a function of substrate stiffness. In this article we analyze the respective role of cell shape and substrate stiffness on actin ordering and show that they both contribute to drive cell polarity.

II. EXPERIMENT

In order to determine if cell shape, actin polarization, and substrate stiffness are related, we used microcontact printing to confine rat embryonic fibroblast cells (REF52) in fibronectin-coated adhesive regions of defined shapes on micropillar substrates as described previously [19] [see Fig. 1(a) and the Appendix]. The use of micropillar substrates enabled us to precisely control the stiffness and measure cellular traction forces; substrates of stiffnesses 9, 38, and 85 nN μm^{-1} were used to mimic soft, intermediately stiff, and very stiff ECMs, respectively [13]. We used shapes of the same area (approximately equal to 3000 μm^2) that appear like ice cream cones with varying apex angles to mimic front-rear polarized states of the cells [6,7] [see Fig. 1(b) and the Appendix]. The shapes were named circle, cone120, cone60, and cone30, where numbers refer to the apex angle for conical shapes in degrees.

We first examined the dynamics of the actin cytoskeleton. If the actin filaments flow freely within the cell, they would be unable to engage with, and anchor, the substrate through FAs [20]. This would prevent FA-mediated signaling, as well as stabilization and polarization of the cytoskeleton. Previously, we had observed that the actin cytoskeleton is fluidlike on soft substrates (9 nN μm^{-1}) and solidlike on stiff substrates (85 nN μm^{-1}), which was interpreted as an increase of the characteristic viscoelastic timescale of the actin cytoskeleton with rigidity; however, elongated cells on soft substrates were not fluidlike [13]. Thus, we imaged live cells adhering to the circular pattern on 9- and 85-nN μm^{-1} substrates to decouple the effects of substrate stiffness and cell shape on actin cytoskeleton fluidity [21]. Similar to our previous observations, we found that the circular cells on 9-nN μm^{-1} substrates exhibited an orthoradial organization of the actin cytoskeleton, whereby the transverse fibers flowed centripetally from the cell boundary towards cell center [Figs. 2(a) and 2(c)]. The flow was observed both at the cell boundary and inside the cell

*Present address: Department of Biomedical Engineering and Biological Design Center, Boston University, Boston, MA 02215, USA.
†Corresponding author: raphael.voituriez@upmc.fr
‡Corresponding author: benoit.ladoux@ijm.fr

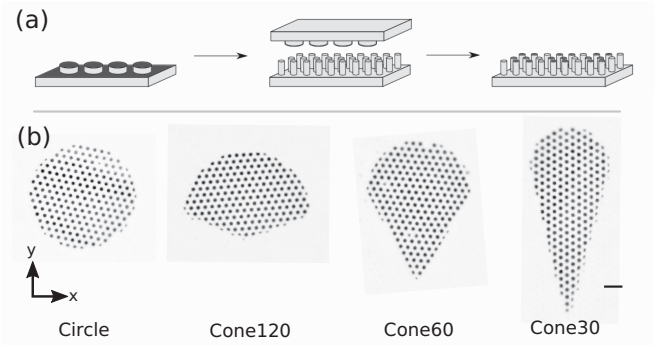

FIG. 1. Patterned printing of cell adhesion protein on micropillars. (a) Schematic showing microcontact printing of cell adhesion protein (fibronectin) in patterns. (b) Fluorescence images of micropillar tops with fibronectin patterned in different shapes with area approximately equal to 3000 μm^2. The scale bar is 10 μm.

bulk. In contrast, circular cells on the 85-nN μm^{-1} substrate had well-aligned stress fibers that showed no flow in the cell bulk [Figs. 2(b) and 2(d)] and only short-range flows along the cell boundary due to classical retrograde flow driven by cellular protrusions [22]. These observations show that a soft substrate is necessary for the fluidity of the cytoskeleton for circular cell shapes. Thus, our previously observed transition of actin cytoskeleton from fluidlike to solidlike behavior and the consequent cell polarity would be primarily dependent on the substrate stiffness.

We next stained actin filaments to analyze the organization of the cytoskeleton on different shapes and stiffnesses. We calculated the cell-averaged nematic order parameter $\langle S\rangle = \langle\cos 2\theta\rangle$, weighted by filament intensity, where θ is the filament angle from the x axis [x-axis definition in Fig. 1(b)]. Our definition of $\langle S\rangle$ here with fixed reference axis leads to $\langle S\rangle > 0$ for x-axis alignment and $\langle S\rangle < 0$ for y-axis alignment; this differs from the classical definition that leads to $\langle S\rangle > 0$ irrespective of alignment. Note that cells in circle patterns were rotated such that $\langle\theta\rangle = 0$. Also, although individual actin filaments are polar in nature, stress fibers, which are bundles of antiparallel actin filaments, are apolar in nature and thus undergo nematic ordering.

We found that on 9-nN μm^{-1} substrates there were no thick bundles of actin filaments for all cell shapes [Figs. 3(a)–3(d)]. We observed only thin bundles which were excluded from the bulk (center) of the cell body and mostly aligned along the cell boundaries, irrespective of cell shape (Fig. 4). On intermediately stiff 38-nN μm^{-1} substrates, we observed stress fibers that were aligned in locally well-ordered domains for all cell shapes [Figs. 3(e)–3(h)]. The stress fiber microdomains preferentially aligned with the nearest straight cell boundary; thus the actin cytoskeleton was ordered at the subcellular scale but not at the cellular scale. This led to overall larger values of $|\langle S\rangle|$, however, with important cell-to-cell variability due to fluctuations in numbers and shapes of domains. On 85-nN μm^{-1} substrates, the stress fibers were mostly aligned in the bulk irrespective of boundary [Figs. 3(i)–3(l) and 4], leading to larger values of $|\langle S\rangle|$ on all shapes. Generally, for a given cell shape $|\langle S\rangle|$ increased on stiffer substrates, and for a given stiffness $|\langle S\rangle|$ increased on more polarized shapes. Although we had shown previously as well that actin filaments increasingly align in the cell bulk with increasing ECM stiffness [13], our current observations show that this increase in bulk alignment does not depend on the cell shape. Thus, we concluded that the cell boundary acts as an anchor for the filaments close to it, while the ECM stiffness influences the alignment of actin filaments in the bulk of the cell.

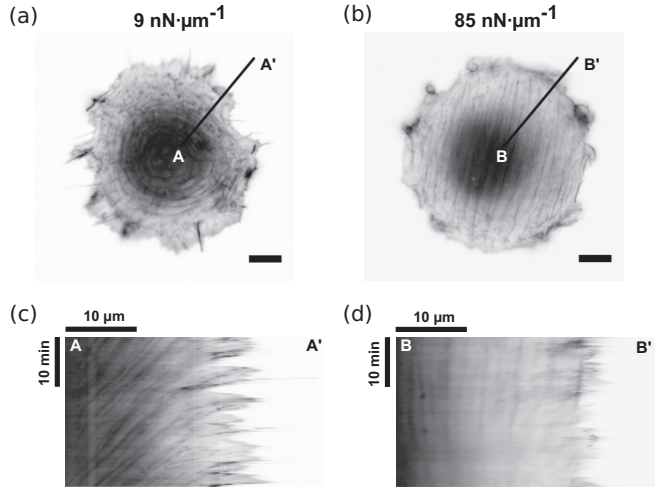

FIG. 2. Actin cytoskeleton fluidity depends on ECM stiffness and not cell shape. A live-cell image of the REF52 cell is shown on (a) soft (9 nN μm^{-1}) and (b) stiff (85 nN μm^{-1}) substrates. The cells were transfected with tdTomato–F-tractin to label actin filaments and were cultured on circular shapes. The scale bar is 10 μm. Also shown are kymographs along lines (c) AA$'$ and (d) BB$'$ in (a) and (b), respectively. The cells were imaged every 10 s for 30 min.

III. THEORETICAL MODEL

In order to quantify the relative roles of ECM stiffness and cell shape on the polarization of the actin cytoskeleton, we modeled the cytoskeleton as a two-dimensional anisotropic gel. The orientational ordering of stress fibers comprising the cytoskeleton was measured by the (traceless) nematic order parameter $Q_{ij} = 2S(n_i n_j - \delta_{ij}/2)$, where S is the order parameter amplitude and n_i is the director. Here S and n_i are local quantities, averaged over a small area that contains many filaments; the measurable order parameter $\langle S\rangle$ can then be obtained by averaging over the cell. Following experimental results that suggest a transition from nonpolarized to polarized cells as stiffness increases, we assume that, at the cell scale, the cytoskeleton is close to the isotropic-nematic (I-N) transition [13], thus making both S and Q small. Despite the nonequilibrium nature of the problem, we assume that actin ordering can be obtained from the minimization of an effective energy functional, where (i) ECM stiffness affects the bulk contribution, as found in [13], and (ii) cell shape (anisotropy) enters through boundary terms. This approach may be justified since we are interested in steady states for which the energy minimization reflects balance of torques on the nematic degrees of freedom. Activity might enter phenomenologically in this approach, but understanding how so is beyond the present scope.

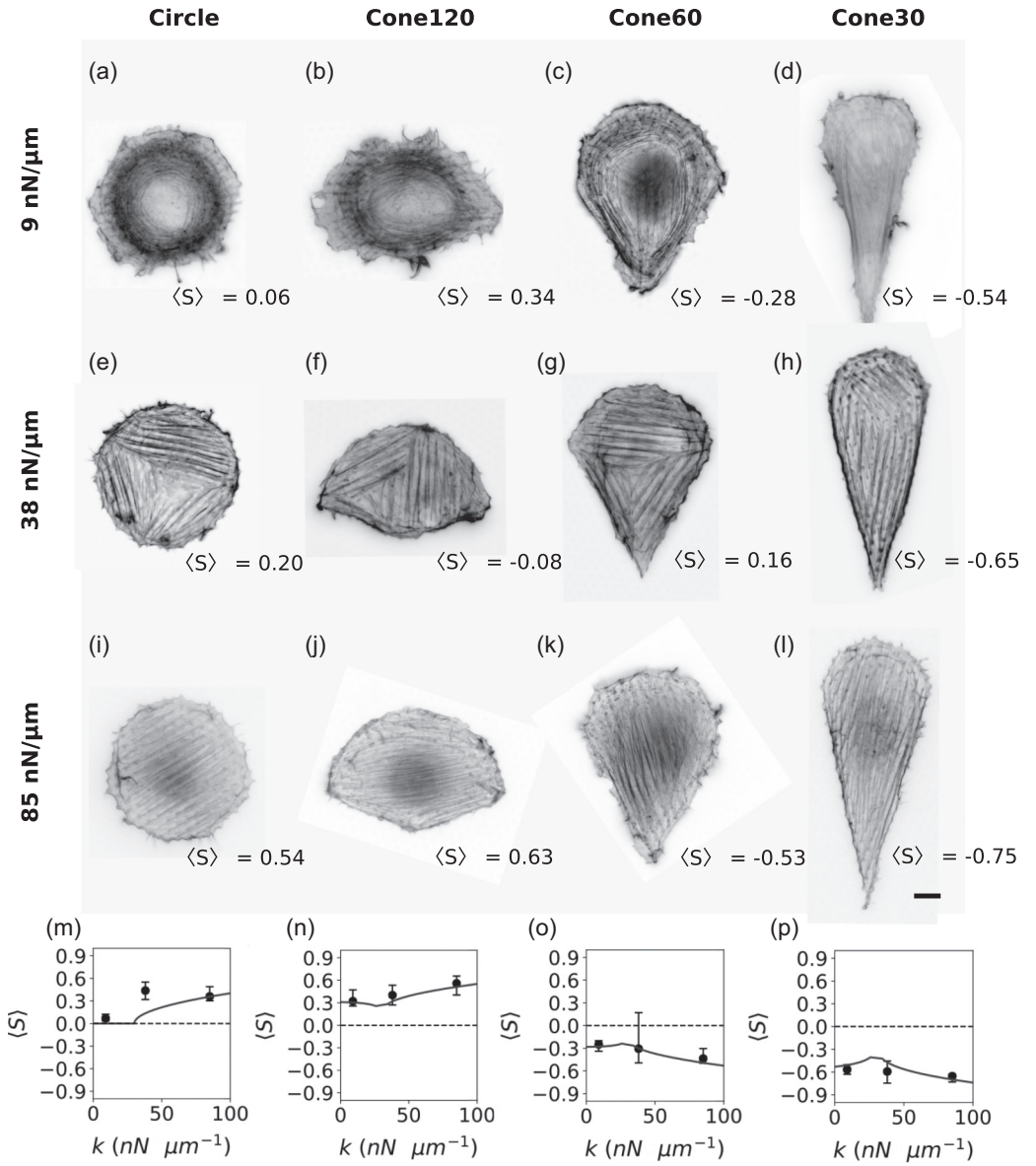

FIG. 3. Actin cytoskeleton organization depends on ECM stiffness and cell shape. (a)–(l) Representative fluorescence images of actin filaments inside cells of different shapes and adhering to micropillar substrates with stiffness as indicated. The scale bar is 10 μm. (m)–(p) Order parameter $\langle S\rangle$ of the actin cytoskeleton for cells adhering to different substrate stiffnesses (9, 38, and 85 nN μm^{-1}) and in different shapes (circle, cone120, cone60, and cone30, respectively). Each data point represents median values obtained from 24–86 cells. The error bar ends represent first and third quartiles of the data. Theoretical fits were obtained from Eq. (7) using $k^* = 30$ nN μm^{-1} [13], $L\sqrt{\omega/\lambda} = 10$, $\gamma_0'/\omega = 2.32$ m N^{-1}, and $w/\sqrt{\lambda\omega} = 0.57$; m was calculated as 0, 0.17, −0.14, and −0.62 for circle, cone120, cone60, and cone30, respectively, using Eqs. (5) and (6). Here $a = \gamma_0'/\omega$ and $b = w/\sqrt{\lambda\omega}$ were the only parameters required to fit all the experimental data ($R^2 = 0.73$); $L\sqrt{\omega/\lambda}$ was only used to remove divergence at $k = k^*$. The 95% confidence intervals for the degree of influence of stiffness a and for the degree of influence of shape b are $1.66 < a < 2.97$ and $0.42 < b < 0.72$, respectively.

More explicitly, in two dimensions the bulk nematic energy is given generically by the Landau–de Gennes expression

$$F_b = \int \left\{ \frac{\gamma}{2}\mathrm{Tr}(\mathbf{Q}^2) + \frac{\omega}{4}[\mathrm{Tr}(\mathbf{Q}^2)]^2 + \frac{\lambda}{2}(\nabla\mathbf{Q})^2 \right\} dA, \quad (1)$$

where γ, $\omega > 0$, and $\lambda > 0$ are constants and integration is performed over the cell area. In the isotropic phase, $\gamma > 0$, while in the nematic, $\gamma < 0$. Previously, we had found that γ decreases with ECM stiffness [13]. By analogy with lyotropic nematics [13,23], this was argued to be a consequence of the dependence of γ on density and the active densifying response of the cytoskeleton to substrate stiffness [13]. We next add to this bulk energy the contribution of a boundary term, which can be written on general grounds

$$F_a = w \oint \mathbf{N}\cdot\mathbf{Q}\cdot\mathbf{N}\, dl, \quad (2)$$

where $\mathbf{N}$ is the unit normal to the cell boundary curve and dl is the infinitesimal arc length along the cell contour. The anchoring strength $w > 0$ favors anchoring of fibers parallel to the boundary (planar anchoring), while $w < 0$ favors normal anchoring. In the isotropic phase, the boundary term favors

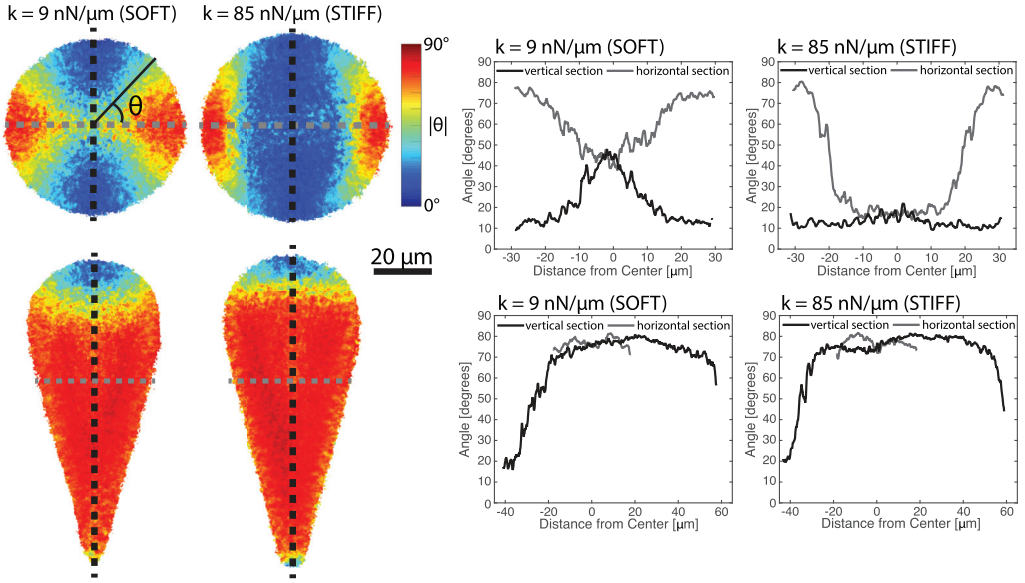

FIG. 4. Median actin distributions on soft and stiff patterns. On the left are maps showing the median angle of actin with respect to the horizontal axis for soft (left) and stiff (right) circles (top) and 30° degree cones (bottom). For circles, the cells are rotated such that the average angle of actin is in the horizontal direction, while cells on cones are aligned to the shape of the pattern. On the right are line scans along the corresponding angle maps in the vertical (black) and horizontal (gray) directions (also shown overlayed on angle maps). The median angle of actin is more likely to be aligned with the nearest boundary on soft patterns than on stiff patterns, which results in more orthoradial actin cables on soft circles and more polarized actin in the conical shape. In round regions of the patterns, the influence of the cell boundary decays more quickly on stiff patterns.

a finite value S_0 of the order parameter, which decays away from the cell edge over the correlation length $\xi_0 = \sqrt{\lambda/|\gamma|}$ [24]. For convenience, in a finite cellular system of typical size L, we introduce $\xi = \min(\xi_0, L)$.

To study the competition between bulk and boundary energies, we develop a mean-field analysis of the model and average S over a thin rectangular region, of width dl and depth L (cell scale). We assume that the boundary value is S_0, which for the moment is unspecified, and that S decays to its bulk value S_b inside the cell [with $S_b = 0$ in the I phase and $S_b = O(|\gamma|^{1/2})$ in the N phase]:

$$\langle S\rangle_{dl} = \frac{1}{L}\int_0^L (S_0 - S_b)e^{-x/\xi}dx + S_b \sim \frac{\xi}{L}S_0, \tag{3}$$

where $\sim$ means lowest order in γ. Then, averaging over the cell contour, we obtain $\langle S\rangle \sim \frac{\xi}{L}\langle S_0\rangle$, where $\langle S_0\rangle$ is the contour average of S_0. Similarly, we obtain $\langle \mathsf{Q}\rangle \sim \frac{\xi}{L}\langle \mathsf{Q}_0\rangle$, with Q_0 the boundary value of the order parameter tensor (the bulk value, of order $|\gamma|^{1/2}$ in the N phase, is neglected). As a result, the mean-field energy (per unit area) is given by

$$\mathcal{F} = \left[\frac{\gamma}{2}\langle S\rangle^2 + \frac{\omega}{4}\langle S\rangle^4\right] + \frac{w}{L^2}\oint \mathbf{N}\cdot\langle \mathsf{Q}_0\rangle\cdot\mathbf{N}\,dl \simeq \left[\frac{\gamma}{2}\langle S\rangle^2 + \frac{\omega}{4}\langle S\rangle^4\right] + \frac{w}{\xi}\mathrm{Tr}(\langle \mathsf{Q}\rangle\cdot\tilde{\mathsf{M}}), \tag{4}$$

where

$$\tilde{M}_{ij} = \frac{1}{L}\oint N_i N_j dl \tag{5}$$

is a purely geometric quantity that describes the cell shape and acts as an aligning field on $\langle \mathsf{Q}\rangle$. The mean-field values of $\langle S\rangle$ and $\langle \mathsf{Q}\rangle$ are then found by minimizing $\mathcal{F}$. We note that the principal axes of $\langle \mathsf{Q}\rangle$ coincide with those of $\tilde{\mathsf{M}}$, while also corresponding to the cell symmetry axes. Finally, $\langle \mathsf{Q}\rangle$ only couples to the traceless part of $\tilde{\mathsf{M}}$, denoted by M. In the diagonal basis (x, y) (Fig. 1) these tensors can be written as

$$\mathsf{M} = \begin{pmatrix} -m & 0 \\ 0 & m \end{pmatrix}, \quad \langle Q\rangle = \begin{pmatrix} \langle S\rangle & 0 \\ 0 & -\langle S\rangle \end{pmatrix}. \tag{6}$$

With this convention, $\langle S\rangle > 0$ indicates alignment along x and $\langle S\rangle < 0$ along y. Finally, minimizing $\mathcal{F}$ yields

$$\gamma\langle S\rangle + \omega\langle S\rangle^3 - \frac{2wm}{\xi} = 0, \tag{7}$$

where $\gamma = \gamma_0'(k^* - k)$ [13], which explicitly determines $\langle S\rangle$. Here k is the substrate stiffness and k^* its critical value at which the I-N transition occurs. If the cytoskeleton is away from the I-N transition ($\gamma \neq 0$) in the isotropic phase, then

$$\langle S\rangle \simeq \frac{2wm}{\gamma\xi} \propto \frac{1}{\sqrt{\gamma}}. \tag{8}$$

Thus, $\langle S\rangle$ increases with increasing cell anisotropy (m) and increasing substrate stiffness (translating into lower γ).

IV. DISCUSSION

The above analysis qualitatively accounts for our results presented in Figs. 3(a)–3(l). Using Eqs. (5) and (6), the cell anisotropy m was calculated as 0, 0.17, −0.14, and −0.62 for the shapes circle, cone120, cone60, and cone30, respectively; positive values indicate that the major axis of the shape is along the x axis, while negative values indicate the y axis. We

first note that, as predicted, actin filament alignment follows the major axis of the cell shape imposed by the pattern, as shown in Figs. 3(a)–3(l), which indicates that the cell shape anisotropy predetermines the direction of actin filament alignment. Second, from Eq. (7) we find that the anchoring strength w is positive, which implies planar anchoring at the cell boundary, as is observed. Third, our theoretical values for $\langle S\rangle$, as obtained from Eq. (7), fit well with the experimental data and reproduce the increase of the order parameter with substrate stiffness and shape anisotropy. Finally, we note that the analogy of this theoretical approach with the classical Landau theory of second-order phase transitions makes it possible to quantify the relative importance of boundary and bulk contributions to ordering. The response to shape anisotropy can be quantified by the susceptibility $\partial\langle S\rangle/\partial m \propto 1/\sqrt{\gamma}$, which decreases with increasing stiffness in the N phase, as observed experimentally (Fig. 4). Finally, both our experimental data and theoretical results indicate that both cell boundary shape (or cell anisotropy m) and ECM stiffness (k) cooperatively regulate actin cytoskeleton alignment and polarity.

Finally, we discuss the implications of our results on the force patterns exerted by the cells on their substrate. Tensional homeostasis within cells, or cellular traction forces, is critical for cell migration and has been implicated in maintaining cell polarity [18,25]. It has been shown that traction forces depend on several factors including cell shape, substrate stiffness, actin cytoskeleton organization, and FA morphology [10,13,18,26]. However, cell shape and substrate stiffness are usually coupled and so far it has been difficult to disentangle their relative effects; our approach allows us to do so.

We found that the average force per micropillar was not influenced by the cell shape; rather it depended on the substrate stiffness. The force per pillar increased from around 5 to 15–20 nN as the substrate stiffness increased from 9 to 85 nN μm^{-1} for all four shapes [Figs. 5(a)–5(d)]. This substrate-stiffness-dependent increase in forces is consistent with the hypothesized dependence of γ, and therefore F-actin density, on stiffness. In turn, the order parameter of the force vectors $|S_F|$ showed an increase from the soft to stiff substrates for all shapes except cone30 [see Figs. 5(e)–5(h) and the Appendix], which presents a sharp tip and thus may induce strong alignment even on the soft substrate [as shown in Fig. 3(d)]. The lower $|S_F|$ on stiff cone30 could be due to higher force measurement noise. Overall, our results show a good correlation between the actin filament organization and the spatial distribution of the traction forces, as confirmed by the average force maps [Figs. 5(i)–5(t)], and indicate that the intensity of traction forces is controlled by substrate stiffness, while both cell shape and substrate stiffness impact spatial force patterns.

Finally, our analysis showed quantitatively that both substrate rigidity and cell shape contribute to drive actin organization and cell polarity. While increasing substrate rigidity affects bulk properties of the actin cytoskeleton by favoring long-lived actin stress fibers with increased nematic interactions, cell shape imposes a local alignment of actin fibers to cell edges and yields a purely geometric contribution to actin organization. While both substrate rigidity and cell shape can cooperatively enhance actin ordering for strongly anisotropic shapes, isotropic shapes decrease actin ordering

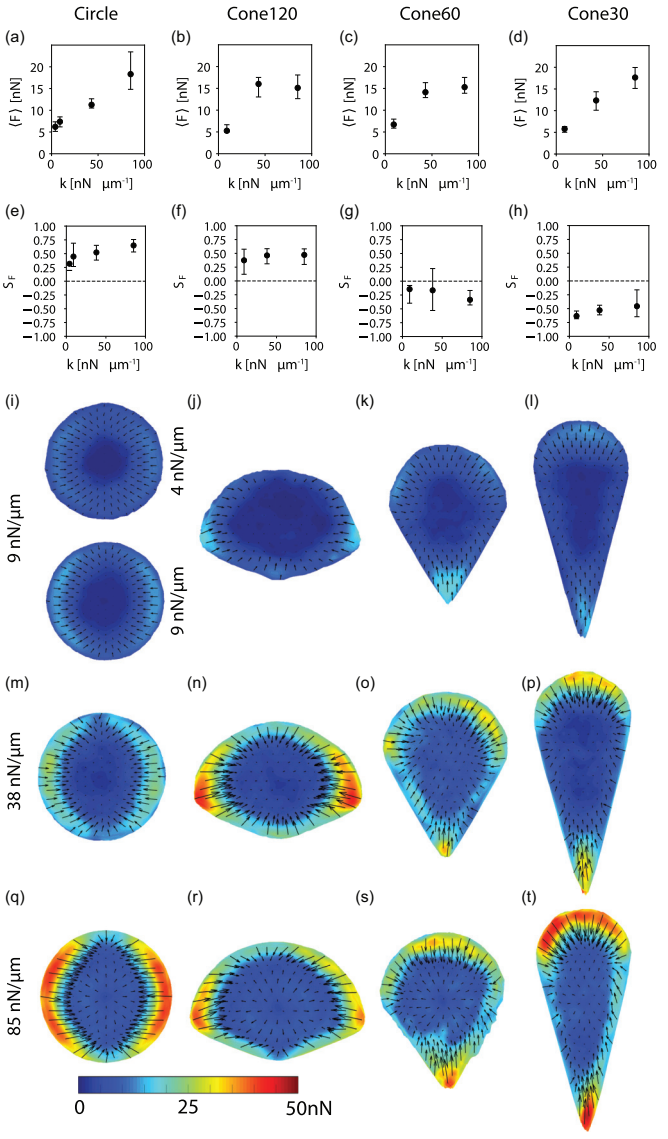

FIG. 5. Cellular traction forces depend on substrate stiffness. (a)–(d) Average traction forces $\langle F\rangle$ applied by cells with the shapes circle, cone30, cone60, and cone120 and adhering to micropillar substrates of stiffnesses 4 (circle only), 9, 38, and 85 nN μm^{-1}. (e)–(h) Order parameter of force vectors S_F. (i)–(t) Average spatial distribution of traction force vectors. Arrows represent force vectors and colors represent force magnitudes in nN. (a)–(t) Data were obtained from 14 to 73 live cells for each condition. (a)–(h) Each data point represents median values and error bar ends represent first and third quartiles of the data.

by imposing conflicting constraints on actin fiber alignment along the cell boundary. This behavior is well captured by a phenomenological model of the actin cytoskeleton, where bulk ordering, characterized by an I-N transition controlled by surface stiffness, and planar anchoring at cell edges, which is shown to act as a purely geometric aligning field, both contribute to drive actin organization at the cell scale.

ACKNOWLEDGMENTS

The authors would like to thank Jacques Prost, Chwee Teck Lim, Bibhu Sarangi, and the group members from Institut

Jacques Monod and Mechanobiology Institute for helpful discussions. Also, the authors thank Gianluca Grenci, Felix Margadant, and the microfabrication core at Mechanobiology Institute. This work was supported by the European Research Council (Grant No. CoG-617233), LABEX "Who Am I?," Agence Nationale de la Recherche "POLCAM" (Grant No. ANR-17-CE13-0013), the USPC-NUS program, and the Mechanobiology Institute.

M.G. and B.L.D. contributed equally to this work.

APPENDIX: METHODS

1. Micropillar fabrication and functionalization

The micropillar substrates were prepared as described previously [13,19]. Briefly, silicon wafers were used to cast polydimethylsiloxane (PDMS) (Sylgard 184, Dow Corning) into micropillars of 2 μm diameter, with heights 3–9 m, resulting in substrate stiffnesses of 9 and 85 nN μm^{-1}. The PDMS (1:10 cross-linker to base polymer ratio) was consistently cured at 80 °C for 2 h to obtain a Young's modulus $E = 2$ MPa. The dimensions of the micropillars were obtained from scanning electron microscope images. The micropillar tops were coated with fluorescent dye-conjugated fibronectin (ATTO647N, Sigma-Aldrich) using microcontact printing technique PDMS stamps with extruded shape patterns (Fig. 6) that were inked with 50 μg ml^{-1} fibronectin and 5 μg ml^{-1} dye-conjugated fibronectin; the stamps were then dried and placed on ultraviolet-ozone treated micropillar substrates for 5 min. The substrates were then immersed in 0.2% Pluronics-F127 solution for 1 h to prevent cell adhesion to the micropillar sides and rinsed with phosphate-buffered saline (PBS). The PBS was then exchanged with the cell culture medium to culture the cells.

2. Cell culture and staining

Rat embryonic fibroblast cells, stably expressing YFP-paxillin, were maintained at 37 °C in a humidified atmosphere of 5% CO_2 and 95% air in Dulbecco's modified Eagle medium containing 10% fetal bovine serum, 100 U/ml penicillin, 100 μg ml^{-1} streptomycin, and 100 μg ml^{-1} glutamine. For live-cell observations of actin cytoskeleton, the cells were transfected with tdTomato–F-tractin using electroporation (Nucleofactor, Lonza) to label actin filaments. Cells on micropillar substrates were fixed 3–4 h after seeding. Cells were fixed for 10 min at room temperature using 4% formaldehyde in PBS, permeabilized using 0.1% Triton-X for 5 min, blocked for 1 h with 1% bovine serum albumin in PBS, and rinsed with PBS. Filamentous actin was stained with 10 mg ml^{-1} Phalloidin-TRITC (Sigma-Aldrich) for 20 min.

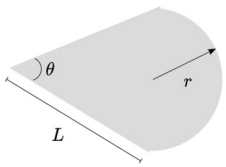

Shape	L (μm)	r (μm)	θ (°)	Area (μm^2)
Circle	—	30	—	2827
Cone120	42	36	120	2842
Cone60	59	30	60	2874
Cone30	90	23	30	2877

FIG. 6. Dimensions of the different shapes used.

3. Imaging

Fluorescent live-cell and fixed-cell images were obtained using an Olympus IX81 inverted epifluorescence microscope equipped with an Olympus UPLSAPO 60× W/1.2 NA objective, a CoolSNAP EZ CCD camera (Photometrics), an X-Cite 120Q fluorescence lamp (Excelitas Technologies), and temperature and CO_2 controller (Life Imaging Sciences). Leibovitz's L-15 cell culture media (Life Technologies) supplemented with 10% fetal bovine serum and 1% penicillin-streptomycin was used for live-cell imaging to minimize background. Live-cell imaging was done in an upside-down configuration as described previously [13,19]. Live cells were imaged 3–7 h after seeding.

4. Order parameter calculation

The order parameter of the actin cytoskeleton is calculated as previously described [13] using a custom-built MATLAB program. Briefly, the local orientation of actin at each pixel is calculated from the local structure tensor of the phalloidin image [27]. The order parameter for each cell is calculated as $\langle S\rangle = \langle\cos 2\theta\rangle$, where θ is angle with the horizontal and averaging is weighted by the fluorescence intensity of the image. Circular patterns are rotated so that $\langle\theta\rangle = 0$. The order parameter of forces was calculated similarly as $\langle S_F\rangle = \langle\cos 2\theta\rangle$, where θ is angle with the horizontal and averaging is weighted by the magnitude of the force vector.

5. Traction force measurements

Live-cell imaging was used to obtain images of deflected micropillars. Traction forces are calculated from micropillar deflections as previously described [13,19] using a custom-built MATLAB program. Briefly, pillar centroids are determined by calculating the center of mass of the pillars following a cross correlation with the expected point spread function of a pillar. Bright-field images are used to determine the orientation and spacing of the undeformed reference lattice of pillars around the cell and then this reference lattice is mapped onto fluorescent fibronectin images to determine pillar deflection magnitudes. Forces are calculated by multiplying the pillar deflection with the pillar spring constant. Pillars which are half stamped by fibronectin or collapsed induce artifacts and thus are manually removed. The mean force is calculated using all pillars located underneath the cell. The order parameter of the traction force angles is calculated as $S_F = \langle\cos 2\theta_F\rangle$, where θ_F is the angle of the force vector from the horizontal axis, and averaging of both θ_F and S_F is weighted on the pillar deflection magnitude. Force maps are generated by interpolating the forces on each pillar and then averaging over all cells in the data set. Prior to averaging circular shapes, the cells are rotated such that the average angle of the traction force is aligned in the horizontal direction; for conical shapes the cells are rotated such that the shape is aligned.

[1] J. P. Campanale, T. Y. Sun, and D. J. Montell, J. Cell Sci. **130**, 1201 (2017).
[2] S. W. Grill, P. Gönczy, E. H. K. Stelzer, and A. A. Hyman, Nature (London) **409**, 630 (2001).
[3] C.-P. Heisenberg and Y. Bellaïche, Cell **153**, 948 (2013).
[4] P. Haas and D. Gilmour, Dev. Cell **10**, 673 (2006).
[5] C. M. Franz, G. E. Jones, and A. J. Ridley, Dev. Cell **2**, 153 (2002).
[6] X. Jiang, D. A. Bruzewicz, A. P. Wong, M. Piel, and G. M. Whitesides, Proc. Natl. Acad. Sci. USA **102**, 975 (2005).
[7] M. Théry, V. Racine, M. Piel, A. Pépin, A. Dimitrov, Y. Chen, J.-B. Sibarita, and M. Bornens, Proc. Natl. Acad. Sci. USA **103**, 19771 (2006).
[8] S. Tojkander, G. Gateva, and P. Lappalainen, J. Cell. Sci. **125**, 1855 (2012).
[9] B. Ladoux, R.-M. Mège, and X. Trepat, Trends Cell Biol. **26**, 420 (2016).
[10] L. Trichet, J. Le Digabel, R. J. Hawkins, S. R. K. Vedula, M. Gupta, C. Ribrault, P. Hersen, R. Voituriez, and B. Ladoux, Proc. Natl. Acad. Sci. USA **109**, 6933 (2012).
[11] M. Prager-Khoutorsky, A. Lichtenstein, R. Krishnan, K. Rajendran, A. Mayo, Z. Kam, B. Geiger, and A. D. Bershadsky, Nat. Cell Biol. **13**, 1457 (2011).
[12] M. J. Dalby, M. O. Riehle, H. Johnstone, S. Affrossman, and A. S. G. Curtis, Biomaterials **23**, 2945 (2002).
[13] M. Gupta, B. R. Sarangi, J. Deschamps, Y. Nematbakhsh, A. Callan-Jones, F. Margadant, R.-M. Mège, C. T. Lim, R. Voituriez, and B. Ladoux, Nat. Commun. **6**, 7525 (2015).
[14] B. R. Sarangi, M. Gupta, B. L. Doss, N. Tissot, F. Lam, R.-M. Mége, N. Borghi, and B. Ladoux, Nano Lett. **17**, 399 (2017).
[15] A. Elosegui-Artola, R. Oria, Y. Chen, A. Kosmalska, C. Pérez-González, N. Castro, C. Zhu, X. Trepat, and P. Roca-Cusachs, Nat. Cell Biol. **18**, 540 (2016).
[16] W. R. Legant, J. S. Miller, B. L. Blakely, D. M. Cohen, G. M. Genin, and C. S. Chen, Nat. Methods **7**, 969 (2010).
[17] S. J. Han, K. S. Bielawski, L. H. Ting, M. L. Rodriguez, and N. J. Sniadecki, Biophys. J. **103**, 640 (2012).
[18] P. W. Oakes and M. L. Gardel, Curr. Opin. Cell Biol. **30**, 68 (2014).
[19] M. Gupta, L. Kocgozlu, B. R. Sarangi, F. Margadant, M. Ashraf, and B. Ladoux, Methods Cell Biol. **125**, 289 (2015).
[20] L. B. Case and C. M. Waterman, Nat. Cell Biol. **17**, 955 (2015).
[21] See Supplemental Material at http://link.aps.org/supplemental/10.1103/PhysRevE.99.012412 for a video showing actin cytoskeleton fluidity.
[22] J. A. Theriot and T. J. Mitchison, Nature (London) **352**, 126 (1991).
[23] P. G. de Gennes and J. Prost, *The Physics of Liquid Crystals* (Oxford University Press, Oxford, 1995).
[24] G. Skačej, A. L. Alexe-Ionescu, G. Barbero, and S. Žumer, Phys. Rev. E **57**, 1780 (1998).
[25] S. L. Gupton and C. M. Waterman-Storer, Cell **125**, 1361 (2006).
[26] N. Q. Balaban, U. S. Schwarz, D. Riveline, P. Goichberg, G. Tzur, I. Sabanay, D. Mahalu, S. Safran, A. Bershadsky, L. Addadi, and B. Geiger, Nat. Cell Biol. **3**, 466 (2001).
[27] P. Kovesi, MATLAB and octave functions for computer vision and image processing, available at https://www.peterkovesi.com/matlabfns/.